IEEE Access
Multidisciplinary | Rapid Review | Open Access Journal

Received January 13, 2020, accepted January 20, 2020, date of publication January 23, 2020, date of current version February 4, 2020.

Digital Object Identifier 10.1109/ACCESS.2020.2968964

Dual-Wideband Dual-Polarized Metasurface Antenna Array for the 5G Millimeter Wave Communications Based on Characteristic Mode Theory

BOTAO FENG[1], (Senior Member, IEEE), XIAOYUAN HE[2], JUI-CHING CHENG[3], AND CHOW-YEN-DESMOND SIM[4], (Senior Member, IEEE)

[1]College of Electronics and Information Engineering, Shenzhen University, Shenzhen 518060, China
[2]Beijing Key Laboratory of Network System Architecture and Convergence, Beijing University of Posts and Telecommunications, Beijing 100876, China
[3]Department of Electronic Engineering, National Taipei University of Technology, Taipei 106, Taiwan
[4]Department of Electrical Engineering, Feng Chia University, Taichung 40724, Taiwan

Corresponding author: Chow-Yen-Desmond Sim (cysim@fcu.edu.tw)

This work was supported in part by the International Cooperation Research Foundation of Shenzhen under Grant GJHZ20180418190621167, in part by the Shenzhen Fundamental Research Foundation under Grant JCYJ20170817102315892, and in part by the Shenzhen Science and Technology Program.

ABSTRACT A dual-wideband dual-polarized antenna using metasurface for the fifth generation (5G) millimeter wave (mm-wave) communications is proposed. It is designed and analyzed based on characteristic mode theory (CMT). The proposed metasurface is mainly composed of a 3×3 square-patch, in which its four corner patches are further sub-divided into a 4×4 sub-patch array, while the size of the other four edge patches is reduced and the center patch is etched with a pair of orthogonal slots. By doing so, the side lobe level can be effectively reduced and the main beam radiation can be enhanced. The metasurface is excited by a pair of orthogonally arranged substrate-integrated-waveguide (SIW) to grounded-coplanar-waveguide (GCPW) dual-polarized feeding networks that help to reduce the insertion loss and expand the frequency bandwidth of the feeding ports. In order to yield higher gain, four proposed metasurfaces are fed by a pair of 1-to-8-way power divider feeding networks including a pair of low-transmission-loss E-plane phase shifter. Measured results show desirable impedance bandwidths of 13.85% (24.2-27.8 GHz) and 14.81% (36.9-42.8 GHz) in the lower and upper frequency bands, respectively, and their corresponding average gains are 13.96 and 15.46 dBi.

INDEX TERMS Dual-wideband, dual-polarized, high gain, 5G millimeter wave communications, characteristic mode theory.

I. INTRODUCTION

Due to the outstanding advantages such as miniaturized size, double capacity, eliminating multi-path fading effects, etc., dualband dual-polarized antenna has been widely applied in mobile communications [1]–[3]. Recently, the frequency bands of 24.75-27.5 GHz and 37-42.5 GHz have been preliminarily assigned to the fifth generation millimeter wave communications in China [4]. In the 5G mm-wave communication scenario, to provide high-speed and stable data transmission in a long distance, mm-wave antenna should simultaneously own the excellent characteristics including wide frequency bandwidth, high channel capacity and high gain, etc. [5], [6]. In order to meet the above-mentioned stringent demands, massive efforts have been devoted to 5G mm-wave antenna design, and some outstanding performances have been achieved [7]–[10]. However, up to now, very few literature is available for dual-wideband dual-polarized mm-wave antenna that can be used in the aforesaid 5G dual-wideband mm-wave communications. This is because it is a great challenge for antenna researcher to obtain dual wide bandwidths with a large frequency interval between them in mm-wave frequency band.

The associate editor coordinating the review of this manuscript and approving it for publication was Sudipta Chattopadhyay.

For dual-polarized antenna, there are usually several methods to yield dual-band operation. In [11], by using dual-layer complementary magneto-electric (ME)-dipole structure, dual wide bandwidths of 25.7% (0.78-1.01 GHz) and 45.7% (1.69-2.69 GHz) with high gain of over 8 dBi can be achieved. However, it suffers from a high profile of $0.26\lambda_0$ (λ_0 is the free-space wavelength at the starting frequency). The work in [12] employs two-layer stacked microstrip antenna as well as four meander lines between them, and a low profile of $0.085\lambda_0$ with a band-notch feature can be attained. But, its bandwidth is slightly narrow (3.3-3.7 GHz and 4.7-5.1 GHz). In [13], through introducing the dual opposite-current notches etched on the radiating dipoles, dual bandwidths of 1.68-2.38 GHz and 2.55-3.72 GHz with anti-interference to wireless local area network (WLAN) can be realized. In [14], by exciting both the aperture-shared lower patch and the upper parasitic patch, dual bandwidths covering X-band and S-band (19.3% and 22%) with gain of better than 8.5 dBi can be obtained. Nevertheless, both of the works in [13] and [14] are still unsuitable for 5G mm-wave communications.

Recently, the use of metasurface, which is one kind of two-dimensional metamaterial structure and owns the unique ability of manipulating electromagnetic wave with good results such as broadening bandwidth, gain enhancement, reducing profile and notching frequency band, etc., has attracted extensive interest from the academic and industrial circles [15]. Therefore, many antenna works using metasurface have been reported in the past few years [16]–[19]. In [16], a metasurface antenna that consists of a 4×4 corner-truncated patch array with capacitive loading strips is fed by a slot feeding structure. As a result, an overall size reduction of 63% can be achieved, as compared with the conventional one. In [17], by using a modified cross slot to feed a 4×4-squared-patches metasurface, wide axial-ratio (AR) bandwidth of 31.3% and wide impedance bandwidth of 52.5% can be obtained. In [18], by arranging a metasurface under a substrate-integrated ME dipole antenna, a dual wide bandwidths of 66.7% (3.1-6.2 GHz) and 20.3% (7.1-8.7 GHz) with high gain of over 7.4 dBi can be attained. In [19], by employing a SIW Y-junction cavity-fed dual slot to excite a modified metasurface, dual wide bandwidths covering 23.7-29.2 GHz and 36.7-41.1 GHz are realized in 5G mm-wave communications for the first time.

In this paper, a dual-wideband dual-polarized metasurface antenna with high gain is presented for the 5G mm-wave communications. According to the predicted modal behaviors of metasurface with CMT, by means of splitting the corner patches, reducing the size of the edge patches and etching quasi-cross slots on the center patches of the metasurface, two enhanced radiation modes at 25.5 GHz and 40 GHz can be achieved for dual wideband operation. Furthermore, by employing a pair of orthogonal SIW-to-GCPW transitions and SIW-dual-slot-fed feeding structures to excite the metasurface, dual polarized operation is also achieved. Finally, a pair of orthogonal 1-to-8-way power dividers co-operated with four tri-port E-plane phase shifters are used to drive the four proposed metasurfaces. Notably, the E-plane phase shifters are chosen (instead of applying the modified equal-length unequal-width phase shifter [20]) because they can exhibit good shift phase with lower transmission loss and phase error in the mm-wave band. In this work, high gain of 13.96 dBi and 15.46 dBi for the frequency bands of 24.2-27.8 GHz and 36.9-42.8 GHz can be realized, respectively. To the best knowlege of the authors, it is the first dual-wideband dual-polarized metasurface antenna array using CMT for the 5G mm-wave communications.

II. ANTENNA GEOMETRY AND WORKING MECHANISM

A. CHARACTERISTIC MODE THEORY OF METASURFACE

According to the CMT in [21], the modal significance (MS) and the modal excitation coefficient (V_i) can be defined as follows:

$$MS = \frac{1}{|1 + j\lambda_n|} \tag{1}$$

$$V_i = \int J_n \cdot E_i dS \tag{2}$$

where λ_n, E_i and S represent the eigenvalue of Mode J_n, the impressed E-field, and the surface of conductor area, respectively. Here, the MS describes the modal behaviors without source, while V_i characterizes positioning feeds. In addition, the modal weighting coefficients (a_n) are employed to evaluate the contribution of Mode J_n to the total currents and can be expressed as follows:

$$\begin{aligned} a_n &= \frac{1}{1 + j\lambda_n} \int J_n \cdot E_i dS \\ &= \frac{V_i}{1 + j\lambda_n} \end{aligned} \tag{3}$$

By denoting f_{res} as resonant frequency, based on Eq. (1), $MS(f_{res}) = 1$. If the MS of a characteristic mode at frequency f can be satisfied with the condition as

$$MS(f) \geqslant \frac{\sqrt{2}}{2} \approx 0.707 \tag{4}$$

the characteristic mode can be excited around the frequency f. During the design process, according to the value of $MS(f)$, modal current distributions and radiation patterns of Modes J_n, by choosing suitable Modes J_n and restraining the unwanted ones, good radiation patterns in the desired frequency bands can be excited.

B. ANTENNA ELEMENT DESIGN

In order to design and optimize the antenna with CMT, open boundary is used for surrounding the metasurface, in which the ground plane and substrates are presumed to be infinity in the xoy plane. The configuration and detailed dimensions of the proposed antenna element are shown in Fig. 1 and Table 1, respectively. To obtain good stability, the design is printed on a Rogers RT5880 substrate ($\varepsilon_r = 2.2$ and $\tan\delta = 0.0009$) with thickness of 0.787 mm. Notably, as aforementioned, the proposed metasurface is composed of a 3×3 quasi square

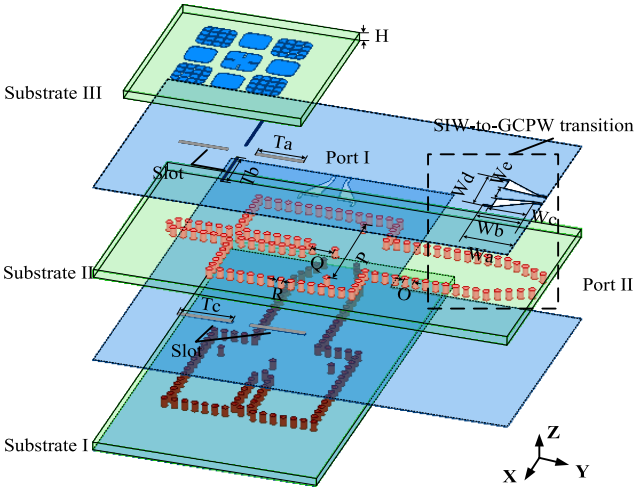

FIGURE 1. Configuration of the antenna element.

TABLE 1. Dimensions for the proposed antenna element.

Parameters	T_a	T_b	T_c	W_a	W_b	W_c	W_d	W_e
Values/mm	3.74	3.88	4.36	4.09	3.22	2.55	4.4	4
Parameters	O	P	Q	R	L_a	L_b	L_c	L_d
Values/mm	0.8	8.72	1.8	0.5	2.66	2.19	2.66	0.59
Parameters	G_a	G_b	H	L_e	L_f			
Values/mm	0.53	0.83	0.787	0.736	0.147			

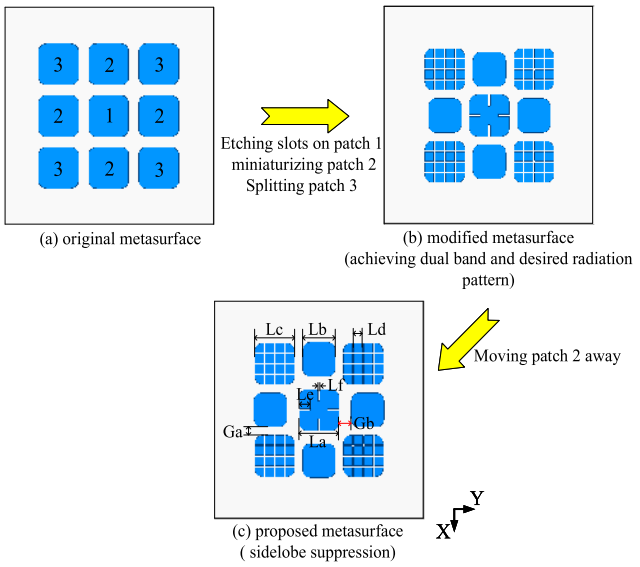

FIGURE 2. Design process of the antenna-element metasurface.

patch, and it is fed by a pair of orthogonal SIW-dual-slot-fed feeding networks.

1) METASURFACE DESIGN

The antenna-element of metasurface is made of thin (35 μm) copper printed on top of the Substrate III, and its design

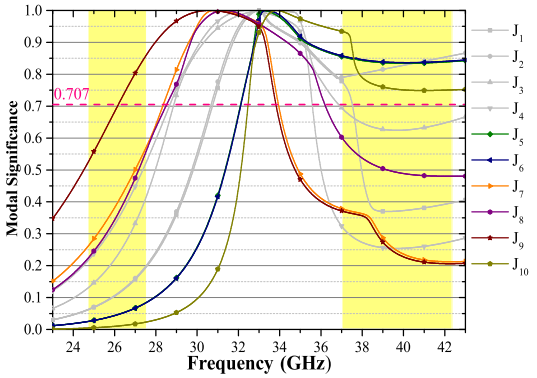

FIGURE 3. MSs of the original metasurface.

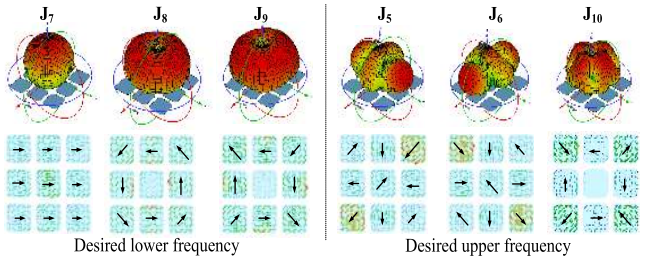

FIGURE 4. Radiation patterns and modal currents of possibly resonant Modes for the original metasurface.

process is shown in Fig. 2. As described in Fig. 2(a), the original metasurface is made up of three kinds of patches, namely, center patch (patch 1), edge patch (patch 2) and corner patch (patch 3). Firstly, by the means of etching a quasi cross slot on patch 1, reducing the size of patch 2, and splitting patch 3 to a 4 × 4 sub array, a preliminarily modified metasurface achieving dual band and desired radiation pattern is shown in Fig. 2(b). Next, by moving patch 2 away from patch 1, the sidelobes of the radiation pattern can be effectively suppressed. In order to understand the design process, Figs. 3-8 depict the operating principle.

The original modal significance (MSs) of the first 10 modes ranging from 23 to 43 GHz are calculated and sorted at 33 GHz with multilayer solver in the electromagnetic simulation software Computer Simulation Technology Suite (CST) [22], as shown in Fig. 3. According to Eq. (4), resonant Modes J_7, J_8 and J_9 maybe induced across the desired lower frequency bands (24.75-27.5 GHz), while resonant Modes J_5, J_6 and J_{10} maybe excited across the desired upper frequency bands (37-42.5 GHz). Other resonant modes J_1-J_4 are the degenerate and undesired modes. The modal currents and radiation patterns of Modes J_5 to J_{10} are depicted in Fig. 4. As observed in the lower frequency bands, if the current intensity on the center patch (patch 1) is weaker than the other one around it (i.e. the current intensity on patches 2 and 3), the radiation patterns of Modes J_8 and J_9 will deteriorate and nulls are formed at boresight direction. In contrast, the radiation pattern of Mode J_7 has exhibited shows good performance. In the upper frequency bands, when the current

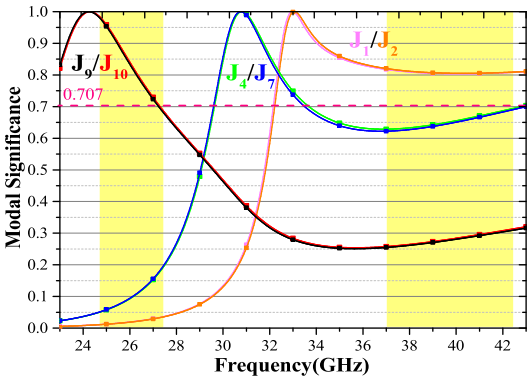

FIGURE 5. MSs of the modified metasurface.

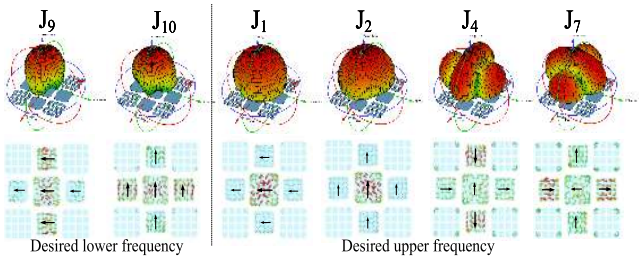

FIGURE 6. Radiation patterns and modal currents of possibly resonant Modes for the modified metasurface.

intensity on the corner patch (patch 3) is larger than others, larger side lobes can be yielded (i.e. the radiation patterns of Modes J_5 and J_6). Similar to Modes J_8 and J_9 in the lower frequency bands, a null is formed at at the boresight direction of Mode J_{10} when the current intensity on the center patch (patch 1) is weaker than the other one around it again. Given all this, the current intensity on the center patch (patch 1) should be enhanced while the others need to be reduced. By these means, good radiation patterns might be excited in our desired frequency bands.

According to these predictions, through etching a quasi cross slot on patch 1, reducing the size of patch 2, and splitting patch 3 into a 4 × 4 sub array, a new MSs is realized, and its corresponding modal currents and patterns of the preliminarily modified metasurface are shown in Figs. 5 and 6, respectively. Here, only the possible resonant Modes (i.e. J_1/J_2, J_4/J_7, and J_9/J_{10}) across the desired frequency bands are selected to be discussed. As seen in Fig. 5, resonant Modes J_9/J_{10} are excited in the desired lower frequency bands, while resonant Modes J_1/J_2 are also excited in the desired upper frequency bands. Notably, the modal currents of Modes J_4/J_7 are similar to the ones of Modes J_1/J_2, and their MSs are close to 0.707, hence they might interfere with the radiations of Modes J_1/J_2. As displayed in Fig. 6, the radiation patterns of J_9/J_{10} and J_1/J_2 show good performance in the desired lower and upper frequency bands, respectively. In comparison, large side lobes are observed in the radiation patterns of J_4/J_7 and they need to be further optimized or removed. As seen from the current distributions on the modified metasurface

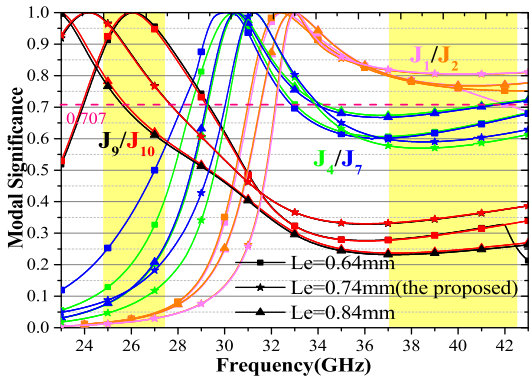

(a) L_e

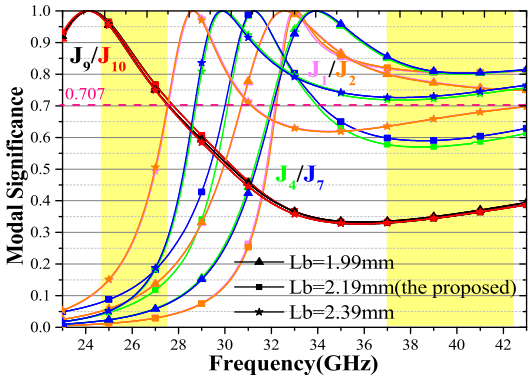

(b) L_b

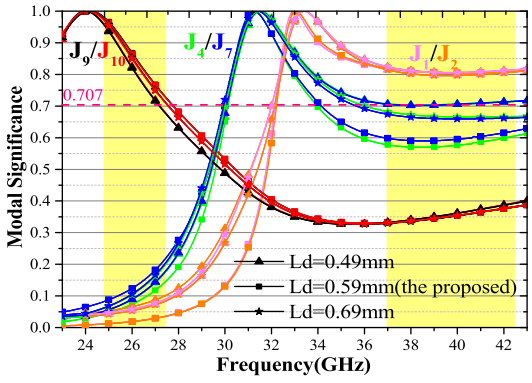

(c) L_d

FIGURE 7. Effects of etching slots on patch 1, reducing size of patch 2 and splitting patch 3.

corresponding to Modes J_4/J_7, the current intensity on the edge patch (patch 2) is much stronger than the one on center patch (patch 1). Furthermore, the stronger current intensity directions of edge patch is opposite to the one of center patch. Therefore, moving the edge patch farther away from the center patch can aid in achieving better radiation patterns.

To further study the effects of the modified and optimized operation, key parameters such as the length of the slot etched on patch 1 (L_e), the side length of patch 2 (L_b), the splitted sub side length of patch 3 (L_d) and the gap length between patch 1 and patch 2 (G_b) are chosen to be investigated, as shown

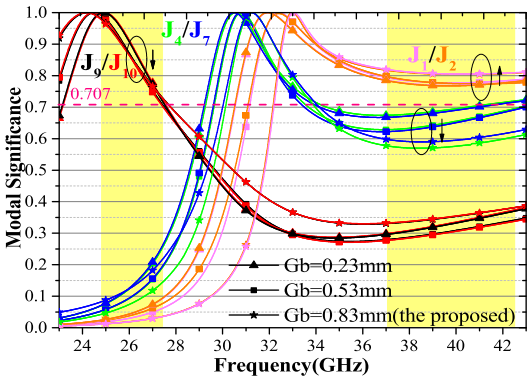

FIGURE 8. Effect of moving away patch 2 (G_b).

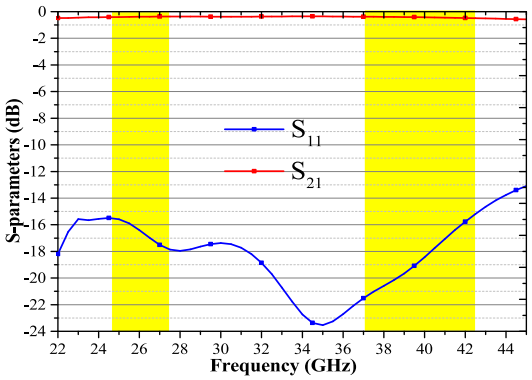

FIGURE 9. The S-parameters of the SIW to GCPW transition.

in Figs. 7 and 8, respectively. Fig. 7(a) shows that as L_e increases from 0.64 mm to 0.84 mm, the MSs of Modes J_4/J_7 is initially reduced ($L_e = 0.74$ mm) but increased when $L_e = 0.84$ mm in the desired upper frequency bands. In comparison, the MSs of Modes J_1/J_2 increases in the desired upper frequency bands, while the MSs of Modes J_9/J_{10} decreases in the desired lower frequency bands. In order to reduce the interference generated by Modes J_4/J_7 in the desired upper frequency bands, and preferably excite both the Modes of J_9/J_{10} in the lower frequency bands and the Modes of J_1/J_2 in the upper frequency bands, $L_e = 0.74$ mm is selected as the optimized value. In comparison with Fig. 7(a), as L_b increases from 1.99 mm to 2.39 mm, Fig. 7(b) shows very little effects on the MSs of Modes J_9/J_{10} across the lower frequency bands. However, in the upper frequency bands, when the value of L_b is selected as 2.19 mm, the desired MSs of Modes J_1/J_2 will yield the largest value and the unwanted MSs of Modes J_4/J_7 get the smallest value. Hence, the side lobes can be suppressed by rescaling the size of the edge patch. Similarly, by changing the value of L_d between 0.49 mm and 0.69 mm, there are hardly any fluctuations with the MSs of Modes J_9/J_{10} in the lower frequency bands and those of Modes J_1/J_2 in the upper frequency bands. In comparison, the MSs of Modes J_4/J_7 will yield the smallest value when L_d is equal to 0.59 mm. It means that by properly splitting the corner patch, the side lobe can also be restrained. As depicted in Fig. 8, as the value of G_b increases from 0.23 mm to 0.83 mm, the MSs of Modes J_9/J_{10} across the lower frequency bands will be slightly smaller, while the ones of Modes J_1/J_2 in the upper frequency bands are moderately large. In comparison, the unwanted MSs of Modes J_4/J_7 in the upper frequency bands become significantly small. In other words, by moving away the edge patch, the side lobe can be obviously reduced.

2) FEEDING NETWORK DESIGN

The SIW feeding structure is employed to drive the metasurface antenna, as shown in Fig. 1. Inspired by [23], [24], the proposed SIW feeding structure mainly comprises of a pair of SIW-to-GCPW transitions, a pair of orthogonal dual-slots, and a pair of 1-to-2-way power dividers. The inner feed line of a coaxial connector is used to connect the center part of the Y-shaped SIW-to-GCPW transition, while its outer grounded lines are used to connect the edge ground of the Y-shaped SIW-to-GCPW transition. By doing so, the bandwidth of the port can be broadened and the insertion loss can also be reduced. Furthermore, compared with the conventional SIW connector, this design has a compact size and is made at a lower cost. Here, the SIW-dual-slot-fed can excite the metasurface to yield the desired resonant modes. Consequently, better dualband impedance bandwidth can be achieved. In our design, one way of the electromagnetic wave is initially fed by port I. Then, it flows along the 1-to-2-way SIW power dividers and is divided into two ways of electromagnetic waves. Finally, the two ways of electromagnetic waves are coupled to the metasurface through the dual-layer dual slots. As a result, dual-wideband operation can be realized along the X-axis polarized direction. Similarly, the other two ways of electromagnetic waves are coupled to the common metasurface through the other orthogonal dual-slots, and another dual-wideband operation can be achieved along the Y-axis polarized direction.

Fig. 9 shows the S-parameters of the SIW to GCPW transition. Here, S_{11} and S_{21} are used to evaluate the port bandwidth and transmission loss, respectively. For a dual-port SIW to GCPW transition, it should simultaneously meet the demands of $S_{21} \geqslant -0.5$ dB and $S_{11} \leqslant -15$ dB in the operating frequency band [25]. As observed, the proposed SIW to GCPW transition can easily satisfy the demand in required 5G dual frequency bands (24.75-27.5 GHz and 37-42.5 GHz).

Fig. 10 shows the current distributions on the metasurface excited by SIW-dual-slot-fed. As observed, at the lower frequency (25.5 GHz), the directions of Port I and Port II are towards the left side and the upper side, respectively. They are orthogonal and corresponding to the modal currents of J_9/J_{10} in Fig. 6. Similarly, at the upper frequency (40 GHz), the directions of Port I and Port II are again towards the left side and the upper side, respectively. They are also orthogonal and corresponding to the modal currents of J_1/J_2 in Fig. 6.

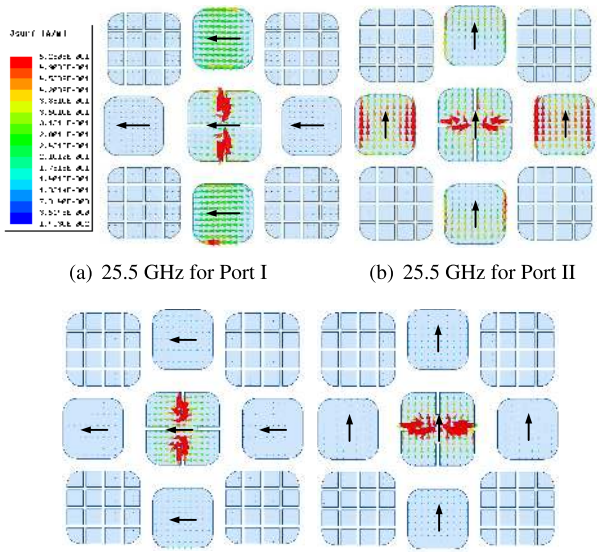

(a) 25.5 GHz for Port I (b) 25.5 GHz for Port II

(c) 40 GHz for Port I (d) 40 GHz for Port II

FIGURE 10. Effects of current distributions on metasurface excited by SIW-dual-slot.

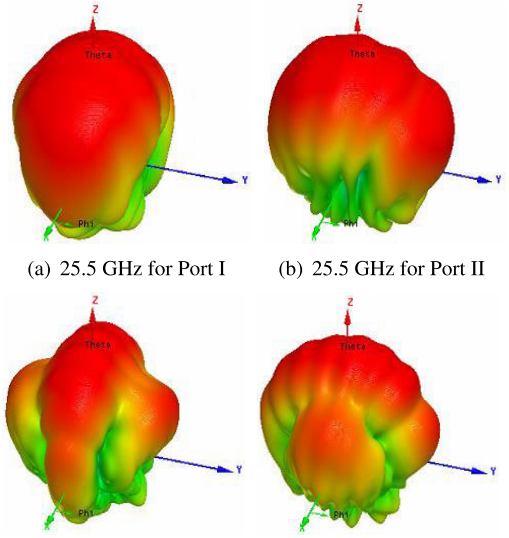

(a) 25.5 GHz for Port I (b) 25.5 GHz for Port II

(c) 40 GHz for Port I (d) 40 GHz for Port II

FIGURE 11. 3D radiation patterns of the final metasurface antenna element.

In other words, by using the SIW-dual-slot-fed, the desired modal radiation can successfully realize dual wide frequency bands with dual polarized directions. To further verify the effect, the corresponding radiation patterns are carried out with electromagnetic simulation software *ANSYS HFSS* [26], as shown in Fig. 11. As easily can be seen, the side lobe can be effectively suppressed and the radiations are mainly towards the boresight direction at both lower and upper frequencies for dual polarizations.

C. ANTENNA ARRAY DESIGN

Based on the antenna element design, a 2 × 2 antenna array is proposed. Its configuration and detailed dimensions are shown in Fig. 12 and Table 2, respectively. In order to provide

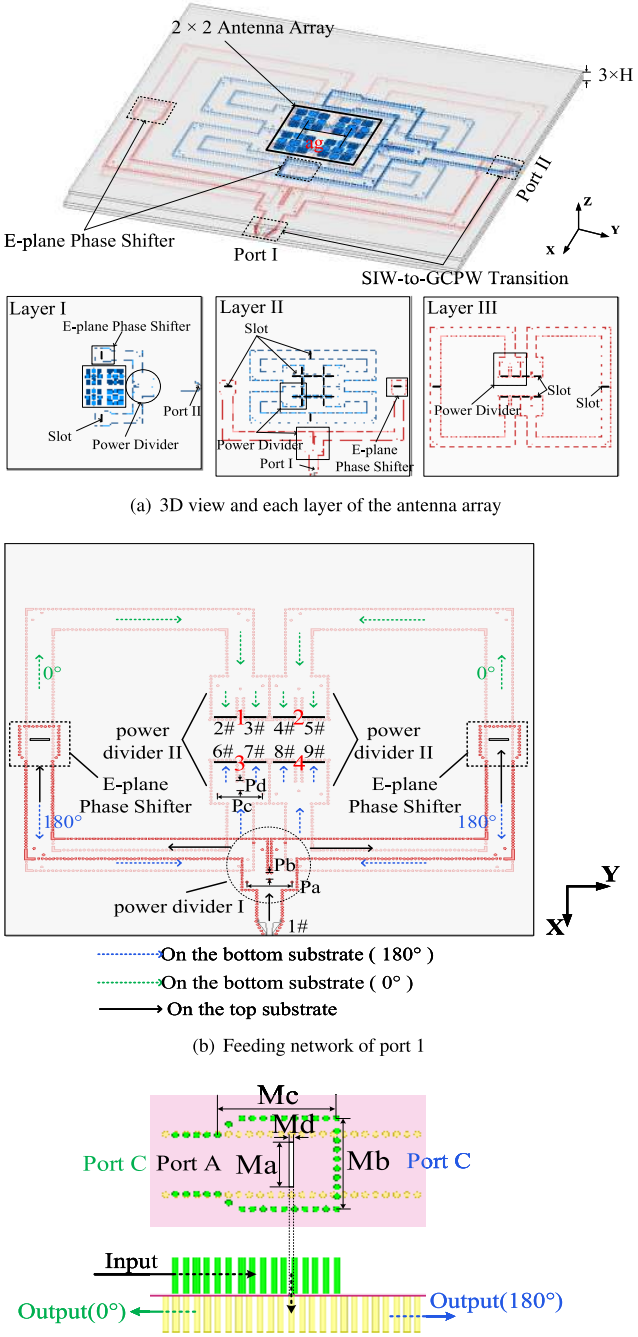

(a) 3D view and each layer of the antenna array

(b) Feeding network of port 1

(c) Configuration of the E-plane phase shifter

FIGURE 12. Configuration of the antenna array.

high gain and high capacity in both polarized directions, four proposed metasurface antenna elements are fed by a pair of modified orthogonal dual-level power divider networks that consist of E-plane phase shifter, as shown in Fig. 12(a).

1) DESIGN OF TWO-LAYER POWER DIVIDER AND E-PLANE PHASE SHIFTER

Here, in order to display the dual-polarized feeding networks clearly and concisely, one way of the feeding network for

TABLE 2. Dimensions for the proposed antenna array.

Parameters	M_a	M_b	M_c	M_d	P_a	P_b	P_c	P_d
Values/mm	7.66	3.79	8.85	0.44	8.81	1.67	8.72	2.4
Parameters	a_g							
Values/mm	11.4							

Port I is selected to be discussed and shown in Fig. 12(b). The input signal that is initially fed by Port I (port 1#) is equally divided into two signals by the first-level power divider (power divider I), follow by flowing into the E-plane phase shifters. Notably, the E-plane phase shifter divides one signal into another two signals with 180°- phase difference. As shown in Fig. 12(c), the proposed E-plane phase shifter consists of the upper and the lower SIW layers. The input signal fed by Port A on the upper layer flows into the lower layer through a slot that connects the upper and lower layers. On the lower layer, the initial signal is divided into two signals with opposite directions. Next, the opposite signals flow to the second-level power divider (power divider II) and are divided into two ways of signals again, as shown in Fig. 12(b). Finally, these signals are coupled to the metasurface through the proposed SIW-dual-slot-fed slots. Consequently, there are periodic oscillating currents on the four metasurfaces along the X-axis direction and one high-gain polarized operation along X-axis can be generated. Similar phenomena are also observed in Port II. Notably, there is not any null with the radiation patterns for the antenna array because there is a 180° phase shift between the feeding of the first and second rows of antenna elements and the current distributions of the antenna elements are the same. In fact, the size of the entire feed network can be further miniaturized for a more compact configuration and a shorter feeding path with a lower insertion loss. However, the bandwidth of the feeding network including the E-plane phase shifter and the power divider will get narrow and cannot cover the desired 5G frequency bands. Taking into account the above-mentioned performance indicators, the proposed size is the optimal value.

2) PERFORMANCE OF TWO-LAYER POWER DIVIDER AND E-PLANE PHASE SHIFTER

Fig. 13 shows the performance of the two-level power divider of the proposed array for Port I. As observed in Fig. 13(a), the phase error between the adjacent front-and-back two ports along the X axis is within ±1° in the dual desired 5G frequency bands. In addition, for a 1-to-8-way power divider, to obtain low transmission loss and wide frequency bandwidth, it should also meet the demand of $S_{11} \leqslant -15$ dB and $S_{1n} \geqslant -9.5$ dB (here, "n" represents the output port number). As shown in Fig. 13(b), the S-parameters of the proposed two-level power divider of the antenna array show good performances and fulfil the requirement with satisfaction.

Simliarly, Fig. 14 shows the performance of the proposed E-plane phase shifter. As shown in Fig. 14(a), the phase error

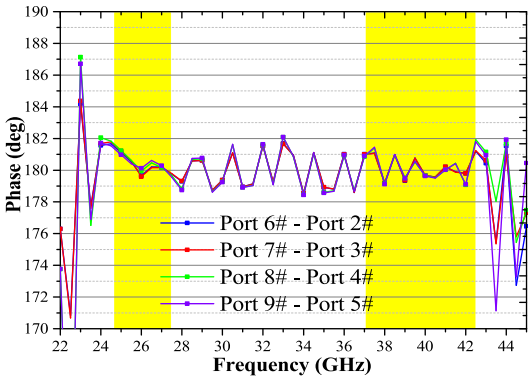

(a) Phase shift

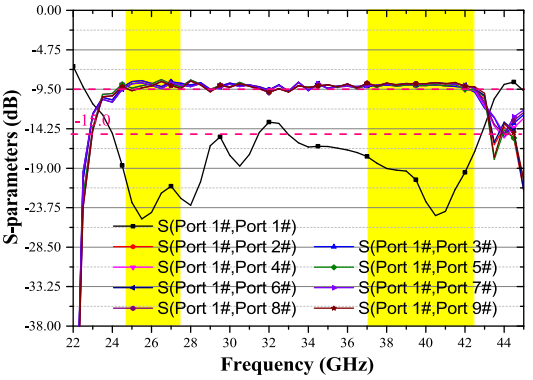

(b) S-parameter

FIGURE 13. Effect of the two-level power divider of the antenna array.

between ports B and C is also within approximately ±1° in the desired frequency bands, which is better than the one (two-layer SIW magic tees) reported in [7] that has ±2.5° phase error. As shown in Fig. 14(b), the values of the transmission curves (S_{BA} and S_{CA}) are larger than −3.5 dB while the values of bandwidth curve (S_{AA}) is lower than −15 dB in the desired frequency bands. These show good performance for a 1-to-2-way E-plane phase shifter.

Fig. 15 exhibits the metasurface current distribution of the antenna array at 25.5 GHz for Port I. It can be obviously observed that the current distributions between the proposed antenna array and the antenna element shown in Fig. 10 are nearly the same. In other words, when the antenna array is formed, the surrounding antenna elements hardly affect the current distributions of one antenna element previously studied.

III. SIMULATED AND MEASURED RESULTS DISCUSSION

To further study the antenna performance, antenna prototypes including antenna element and antenna array are fabricated and measured to verify the proposed model, as shown in Fig. 16. In addition, some key parameters are also simulated to compare with the measured results. In our design, the air gap may cause some energy loss in Port I, whereas it has little impact on Port II (as shown in Fig. 12(a)). In fact, in order to prevent the power leakage between the substrates,

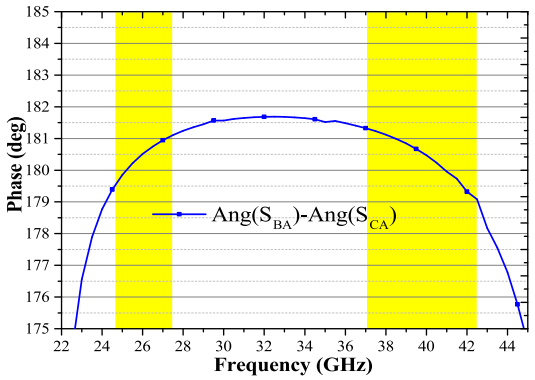

(a) Phase error

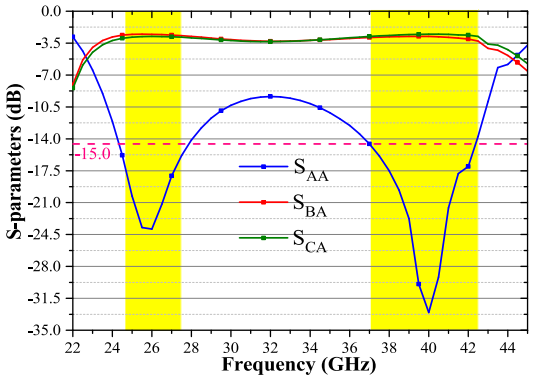

(b) S-parameter

FIGURE 14. Effect of the E-plane phase shifter.

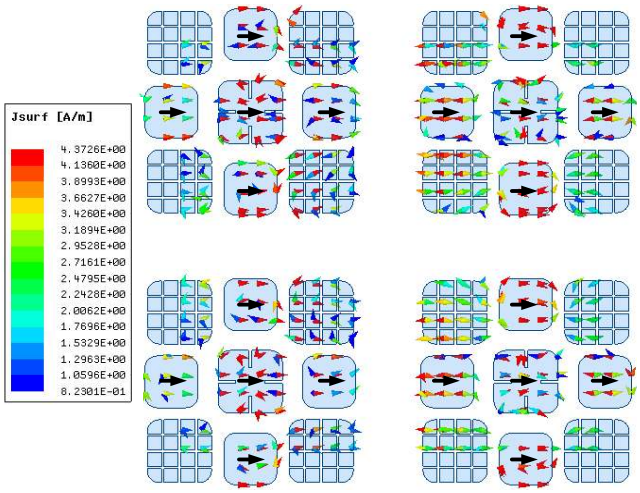

FIGURE 15. Current distribution of the antenna array at 25.5 GHz for Port I.

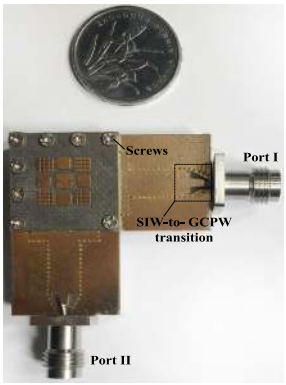

(a) Antenna element

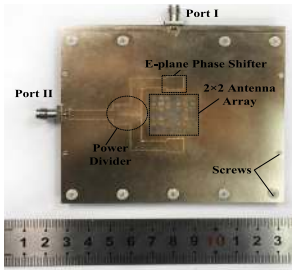

(b) Antenna array

FIGURE 16. Prototypes of the proposed antenna.

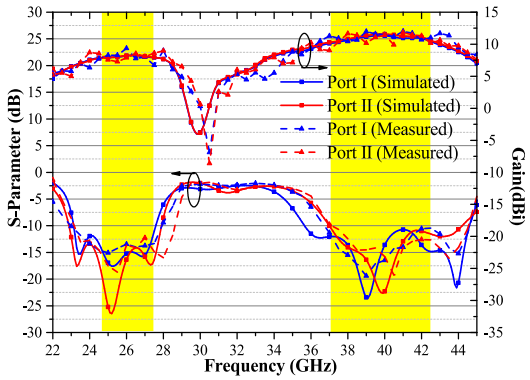

(a) antenna element

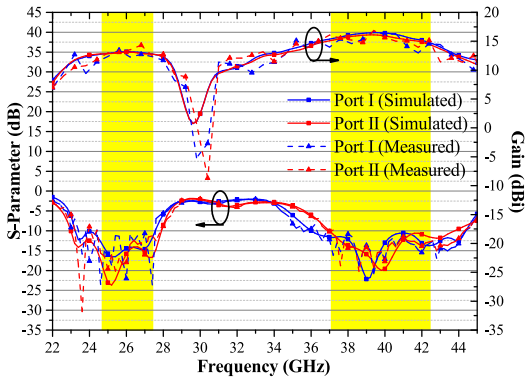

(b) antenna array

FIGURE 17. Simulated and measured S-parameters and gains of both antenna element and antenna array.

many screws have been used for the antenna assembly in the practical fabrication (as shown in Fig. 16). Besides, the simulated and measured S-parameters for the two ports agree each other well. In other words, the number of screws in our design is enough for preventing the influence of the power leakage.

Fig. 17 shows the simulated and measured S-parameters and gains of both antenna element and antenna array. As shown in Fig. 17(a), for the antenna element, the measured overlapped frequency bandwidths are 15.15% (23.8-27.7 GHz) with average gain of 7.69 dB, and 18.72% (36.8-44.4 GHz) with average gain of 10.99 dB in the lower and upper frequency bands, respectively. Similarly, the measured overlapped frequency bandwidths for the antenna array are 13.85% (24.2-27.8 GHz) with average gain of 12.96 dB, and 14.81% (36.9-42.8 GHz) with average gain of 15.46 dB in the lower and upper frequency bands, respectively. In comparison, the measured gains are lower than the simulated ones

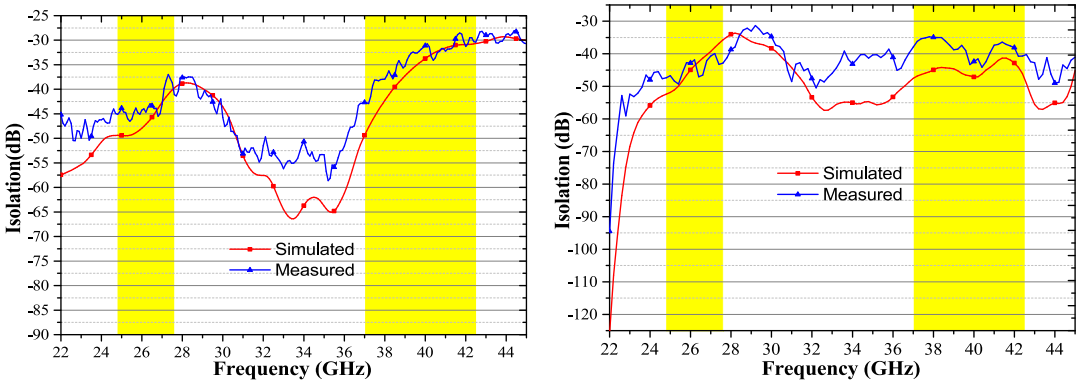

(a) antenna element (b) antenna array

FIGURE 18. Isolation of both antenna element and antenna array.

TABLE 3. Radiation performance of the antenna element at different frequencies.

Parameters	Port I						Port II					
	E-plane			H-plane			E-plane			H-plane		
Frequency (GHz)	HPBW (deg)	X-pol (dB)	FBR (dB)	HPBW (deg)	X-pol (dB)	FBR (dB)	HPBW (deg)	X-pol (dB)	FBR (dB)	HPBW (deg)	X-pol (dB)	FBR (dB)
25.5 (Simulated)	94.0	-27.7	23.3	71.0	-24.6	22.2	65.0	-25.7	22.0	90.8	-23.2	22.0
25.5 (Measured)	90.9	-20.1	19.1	65.9	-22.6	20.1	65.7	-22.6	20.1	90.9	-20.1	19.1
40 (Simulated)	56.0	-27.5	21.1	40.5	-25.1	21.4	40.5	-26.8	21.1	53.1	-28.2	21.0
40 (Measured)	60.2	-24.5	20.4	37.9	-24.1	20.8	37.0	-25.0	19.1	53.0	-24.7	20.2

TABLE 4. Radiation performance of the antenna array at different frequencies.

Parameters	Port I								Port II							
	E-plane				H-plane				E-plane				H-plane			
Frequency (GHz)	HPBW (deg)	Sidelode level (dB)	X-pol (dB)	FBR (dB)	HPBW (deg)	Sidelode level (dB)	X-pol (dB)	FBR (dB)	HPBW (deg)	Sidelode level (dB)	X-pol (dB)	FBR (dB)	HPBW (deg)	Sidelode level (dB)	X-pol (dB)	FBR (dB)
25.5 (Simulated)	23.8	11.4	-23.9	27.1	24.5	10.0	-29.5	24.9	24.9	10.3	-25.5	29.1	24.8	11.4	-36.4	31.5
25.5 (Measured)	22.9	10.1	-23.4	20.6	23.0	9.9	-24.6	24.4	23.0	9.6	-20.5	28.9	23.9	10.7	-26.1	30.9
40 (Simulated)	14.8	8.7	-29.5	23.6	16.8	10.8	-24.8	31.5	16.6	11.8	-21.1	28.3	14.6	8.2	-30.3	28.3
40 (Measured)	13.2	8.3	-25.9	23.4	15.5	10.1	-21.9	29.8	15.6	10.4	-20.5	26.2	13.4	8.0	-21.7	26.2

by about 0.3 dBi for the antenna element, while the measured gains are lower than the simulated ones by approximately 0.5 dBi for the antenna array. This may be caused by the feeding connectors and the cables. On the whole, the measured curves agree well with the simulated ones.

Fig. 18 shows the simulated and measured isolations for antenna element and antenna array. As observed in Fig. 18(a), the measured isolations for the antenna element are less than −35 dB and −28 dB in the desired lower and upper frequency bands, respectively. In comparison, the simulated ones for the antenna element are lower than −40 dB and −32 dB, respectively. Furthermore, as displayed in Fig. 18(b), the simulated isolations of the antenna array for the lower and upper frequency bands are lower than −35 dB and −42 dB, respectively. Correspondingly, the measured ones are less than −40 dB and −42 dB, respectively. Due to the loss incurred by the multi-layer substrate structure, the measured isolations are slightly inferior than the simulated ones. Even so, because the two input ports are orthogonal and their SIWs are printed on different layers, the isolations are much larger than −25 dB and show good polarization purity.

The radiation patterns of the antenna element and the antenna array at different frequencies are shown in

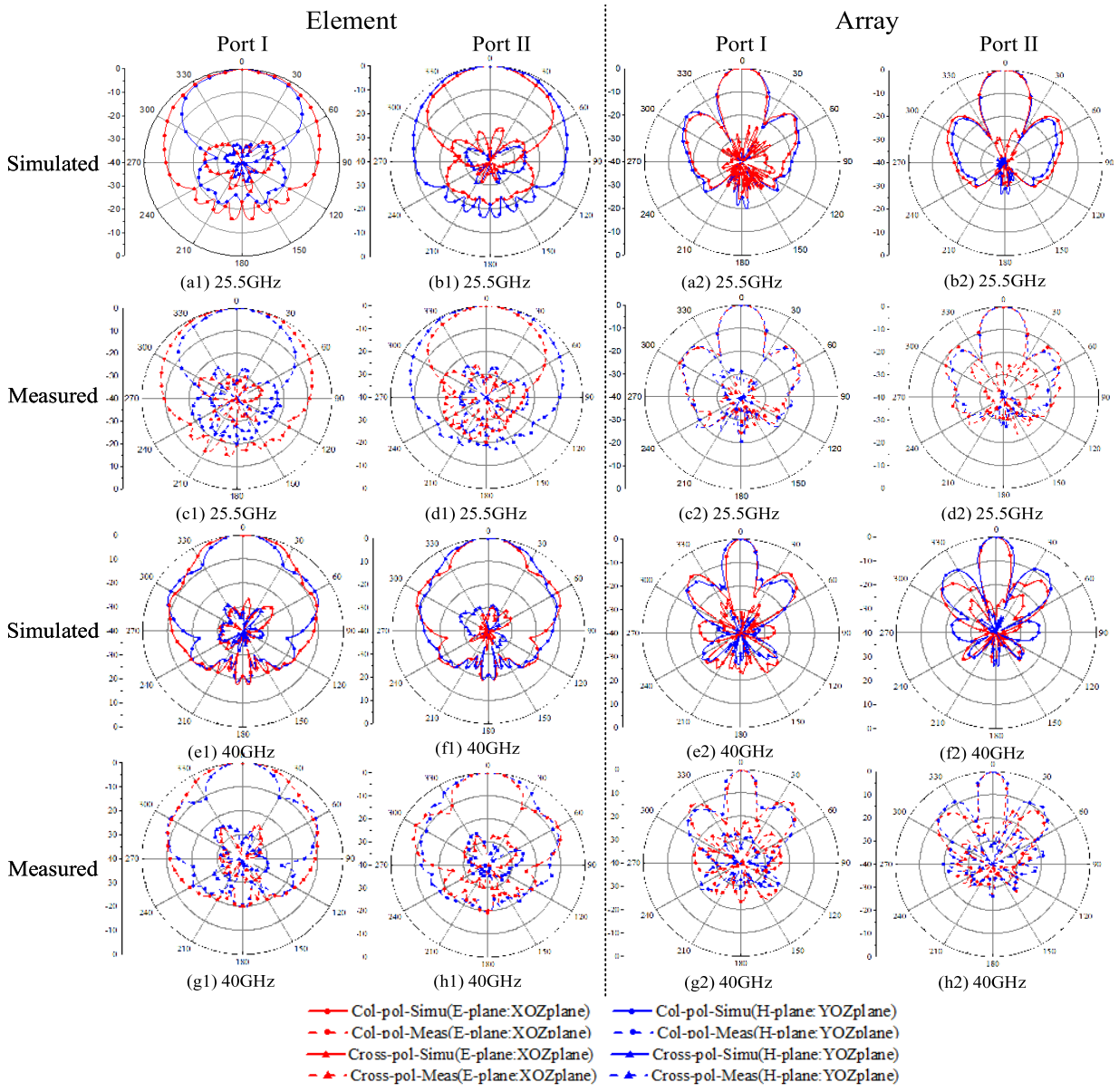

FIGURE 19. Simulated and measured radiation patterns of both antenna element and antenna array.

Fig. 19, and their corresponding characteristics are denoted in Tables 3-4. Owing to the nearly symmetrical structure and low transmission loss design, the simulated radiation patterns between port I and port II are nearly the same as each other. In addition, their radiation patterns are almost symmetrical. For instance, the radiation pattern on E-plane for Port I is almost identical to the one on H-plane for Port II. For the antenna element, its measured cross polarization (X-pol) levels are lower than −20.1 dB, and the measured front to back ratios (FBRs) are larger than 19.1 dB across the whole operating frequency band. Compared with the antenna element, the half-power beamwidth (HPBW) of the antenna array becomes narrower and the side lobe level gets larger. For example, the measured HPBW reaches the smallest value of 13.2° in the E-plane at 40 GHz for port I. Because of the size of the second-level power divider network, the distance between the four metasurfaces cannot be too close. In general, the appropriate center distance between two antenna elements for antenna array is approximately 0.75 λ_c (λ_c is the wavelength corresponding to the center frequency). In our design, the center distance between two neighbouring antenna elements is approximately 0.94 λ_0 (λ_0 is the wavelength corresponding to the starting frequency). As a result, the sidelobe level is slightly large. However, it is still larger than 8 dB and can fulfil the practical applications. In addition, the measured X-pol levels and FBRs are larger than −23.5 dB and 23.4 dB, respectively. In general, the measured values are slightly inferior but close to the simulated ones.

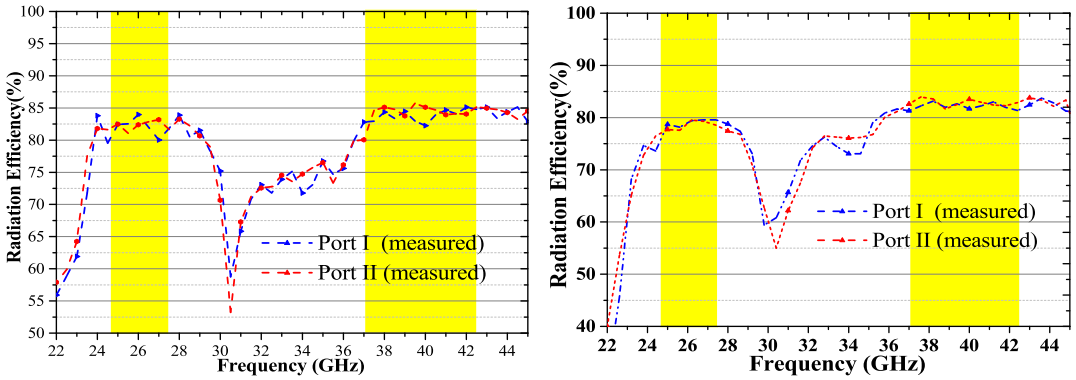

(a) antenna element (b) antenna array

FIGURE 20. Radiation efficiencies of both antenna element and antenna array.

TABLE 5. Comparison of the proposed antenna with other referenced dualband antennas.

Refs.	Element /Array	Numbers of polarization	Bandwidths (Relative BW/GHz)	Average gain (dBi)	Height (λ_0)	Remarks
Element in this work	Element	Dual	15.15% (23.8-27.7 GHz) &18.72% (36.8-44.4 GHz)	7.69 & 10.99	0.202	Dual wideband; Dual polarizations; High gain.
[2]	Element	Dual	5.5% (0.881-0.931 GHz) &59.4% (2.90-5.35 GHz)	1.8 & 2.5	0.29	Dual polarizations; Dual wideband; **Low gain**; **High profile**.
Element in [12]	Element	Dual	11.4% (3.30-3.70 GHz) &5.1% (4.75-5.00 GHz)	8.0 & 10.0	0.085	Dual polarizations; High gain; Low profile; **Narrow bandwidth**.
[19]	Element	Single	20.7% (23.7-29.2 GHz) &11.3% (36.7-41.1 GHz)	6 & 9.9	0.202	Dual wideband; High gain; **Single polarization**.
Element in [27]	Element	Single	1.9% (21.0-21.4 GHz) &2.7% (25.6-26.3 GHz)	10.7 & 11.9	0.072	High gain; **Single polarization**; **Narrow bandwidth**.
Array in this work	Array	Dual	13.85% (24.2-27.8 GHz) &14.81% (36.9-42.8 GHz)	12.96 & 15.46	0.202	Dual wideband; Dual polarizations; High gain.
Array in [12]	Array	Dual	11.4% (3.30-3.70 GHz) &5.1% (4.70-5.00 GHz)	14.5 & 15.5	0.1	Dual polarizations; High gain; Low profile; **Narrow bandwidth**.
Array in [27]	Array	Single	3.8% (20.8-21.6 GHz) &2.7% (25.6-26.3 GHz)	16 & 17.4	0.072	High gain; **Single polarization**; **Narrow bandwidth**.
[28]	Array	Single	12.79% (26.71-30.36 GHz) &5.81% (36.59-38.78 GHz)	10.06 & 10.2	0.062	Low profile; **Single polarization**; **Narrow bandwidth**.

Where λ_0 denotes the free-space wavelength at the starting frequency.

Fig. 20 further shows their radiation efficiencies. For the antenna element, about 83% and 82% radiation efficiencies can be achieved for Ports I and II at the desired lower frequency bands, respectively, while they are approximately 84% and 85% at the upper frequency bands, respectively. In comparison, due to the loss of feeding network, the radiation efficiencies for antenna array are slightly lower than the ones for antenna element. They are approximately 78% and 77% for Ports I and II at the desired lower frequency bands, respectively, and around 82% and 83% at the upper frequency bands, respectively.

Table 5 compares the important characteristics of the proposed antenna with other dualband antennas in the reported references. In [2], by using an U-shaped planar inverted-F antenna to work with a pair of annular dipoles, dual-band and dual polarized features can be attained. However, it suffers from low gain of 1.8 dBi. Through employing a pair of orthogonal differentially driven feeding lines to feed dual-layer stacked patches, the element in [12] obtains duaband and dual polarized features with gain of up to 10 dBi. However, only narrow bandwidths of 3.3-3.7 GHz and 4.75-5 GHz can be achieved. In [19], by introducing an SIW-based dual slot to drive the metasurface, dual wide bandwidths of 23.7-29.2 GHz and 36.7-41.1 GHz with high gain of 4.8-7.2 dBi and 8.9-10.9 dBi can be realized. However, only a single polarization can be achieved. In our design, a dual-polarized dual-band antenna element is initially proposed for high polarization capacity. Next, by using a meticulously designed SIW E-plane feeding network, a 2 × 2 antenna array with high gain and high polarization capacity is presented for practical 5G mm-wave applications. Notably, the sidelobe level in high frequency bands in [19] is large and

hence its gain was degraded. In our design, in order to reduce the side lobe level and enhance the main beam radiation, each of the four corner patches is further divided into a 4×4 patch subarray initially, follow by reducing the size of the other four edge patches and the center patch is etched with a pair of orthogonal slots. In [27], by using a cavity-backed SIW to excite a dual-layer slot antenna, dual high-order radiation modes are generated to reach dualband operation. Nevertheless, its antenna element still suffers from narrow bandwidth and single polarization. Although high gain of over 14 dBi can be achieved, the antenna arrays in [12] and [27] have also exhibited the drawback of narrow bandwidth. In [28], by using a 1-to-4-way power divider network to excite the cavity-backed slot antenna array, dualband operation can be realized in the mm-wave frequency bands. However, only one single polarization can be obtain in the operating bands. In comparison, the antenna element and array in our work can exhibit dual wide impedance bandwidths with high gains (15.15% and 18.72% with gain of 7.69 dBi and 10.99 dBi for element, 13.85% and 14.81% with gain of 12.96 dBi and 15.46 dBi for array) and dual polarization at the same time. Even though the antenna profile is slightly high, it is still lower than 0.202 λ_0.

IV. CONCLUSION

A dual-wideband dual-polarized metasurface antenna with high gain is successfully studied for the 5G mm-wave communications. Based on the CMT, two pairs of characteristic modes at 25.5 and 40 GHz can be enhanced though modifying the metasurface and thus dual wideband operation can be achieved. Furthermore, by employing the orthogonal SIW-to-GCPW transitions and the SIW-dual-slot-fed feeding structure, wide frequency band and low transmission loss characteristics can be obtained in dual polarized directions for the antenna element. Finally, an antenna array that consists of four proposed antenna elements are fed by a meticulously designed 1-to-8-way power divider network to obtain high gain of 13.96 dBi and 15.46 dBi in the desired dual mm-wave frequency bands. With these features, the proposed antenna can be applied in the high-speed and high-capacity 5G communications.

REFERENCES

[1] W. X. An, H. Wong, K. L. Lau, S. F. Li, and Q. Xue, "Design of broadband dual-band dipole for base station antenna," *IEEE Trans. Antennas Propag.*, vol. 60, no. 3, pp. 1592–1595, Mar. 2012.

[2] W. An, Z. Shen, and J. Wang, "Compact low-profile dual-band tag antenna for indoor positioning systems," *IEEE Antennas Wireless Propag. Lett.*, vol. 16, pp. 400–403, 2017.

[3] Y. Cui, R. Li, and P. Wang, "Novel dual-broadband planar antenna and its array for 2G/3G/LTE base stations," *IEEE Trans. Antennas Propag.*, vol. 61, no. 3, pp. 1132–1139, Mar. 2013.

[4] *Chinese Ministry of Industry and Information Technology Allocates Spectrum for the Fifth Gerneration Mobile Communication*. Accessed: Nov. 15, 2017. [Online]. Available: http://www.miit.gov.cn/n1146295/n1652858/n1652930/n3757020/c5907905/content.html

[5] S. Liao and Q. Xue, "Dual polarized planar aperture antenna on LTCC for 60-GHz antenna-in-package applications," *IEEE Trans. Antennas Propag.*, vol. 65, no. 1, pp. 63–70, Jan. 2017.

[6] J. Zhu, Y. Yang, S. Li, S. Liao, and Q. Xue, "Single-ended-fed high-gain LTCC planar aperture antenna for 60 GHz antenna-in-package applications," *IEEE Trans. Antennas Propag.*, vol. 67, no. 8, pp. 5154–5162, Aug. 2019.

[7] J. Zhu, S. Liao, S. Li, and Q. Xue, "60 GHz substrate-integrated waveguide-based monopulse slot antenna arrays," *IEEE Trans. Antennas Propag.*, vol. 66, no. 9, pp. 4860–4865, Sep. 2018.

[8] J. Zhu, S. Li, S. Liao, Y. Yang, and H. Zhu, "60 GHz substrate-integrated-waveguide-fed patch antenna array with quadri-polarization," *IEEE Trans. Antennas Propag.*, vol. 66, no. 12, pp. 7406–7411, Dec. 2018.

[9] A. Li, K.-M. Luk, and Y. Li, "A dual linearly polarized end-fire antenna array for the 5G applications," *IEEE Access*, vol. 6, pp. 78276–78285, 2018.

[10] Y. Li, L. Ge, J. Wang, S. Da, D. Cao, J. Wang, and Y. Liu, "3-D printed high-gain wideband waveguide fed horn antenna arrays for millimeter-wave applications," *IEEE Trans. Antennas Propag.*, vol. 67, no. 5, pp. 2868–2877, May 2019.

[11] B. Feng, S. Li, W. An, W. Hong, and S. Yin, "A differentially driven dual-polarized dual-wideband complementary antenna for 2G/3G/LTE applications," *Int. J. Antennas Propag.*, vol. 2014, pp. 1–10, 2014.

[12] B. Feng, L. Li, J.-C. Cheng, and C.-Y.-D. Sim, "A dual-band dual-polarized stacked microstrip antenna with high-isolation and band-notch characteristics for 5G microcell communications," *IEEE Trans. Antennas Propag.*, vol. 67, no. 7, pp. 4506–4516, Jul. 2019.

[13] B. Feng, L. Li, Q. Zeng, and C.-Y.-D. Sim, "A low-profile metamaterial loaded antenna array with anti-interference and polarization reconfigurable characteristics," *IEEE Access*, vol. 6, pp. 35578–35589, 2018.

[14] K. Wang, X. Liang, W. Zhu, J. Geng, J. Li, Z. Ding, and R. Jin, "A dual-wideband dual-polarized aperture-shared patch antenna with high isolation," *IEEE Antennas Wireless Propag. Lett.*, vol. 17, no. 5, pp. 735–738, May 2018.

[15] D. R. Smith, W. J. Padilla, D. C. Vier, S. C. Nemat-Nasser, and S. Schultz, "Composite medium with simultaneously negative permeability and permittivity," *Phys. Rev. Lett.*, vol. 84, no. 18, pp. 4184–4187, Jul. 2002.

[16] Y. Juan, W. Yang, and W. Che, "Miniaturized low-profile circularly polarized metasurface antenna using capacitive loading," *IEEE Trans. Antennas Propag.*, vol. 67, no. 5, pp. 3527–3532, May 2019.

[17] S. Liu, D. Yang, and J. Pan, "A low-profile broadband dual-circularly-polarized metasurface antenna," *IEEE Antennas Wireless Propag. Lett.*, vol. 18, no. 7, pp. 1395–1399, Jul. 2019.

[18] B. Feng, J. Lai, Q. Zeng, and K. L. Chung, "A dual-wideband and high gain magneto-electric dipole antenna and its 3D MIMO system with metasurface for 5G/WiMAX/WLAN/X-band applications," *IEEE Access*, vol. 6, pp. 33387–33398, 2018.

[19] T. Li and Z. N. Chen, "A dual-band metasurface antenna using characteristic mode analysis," *IEEE Trans. Antennas Propag.*, vol. 66, no. 10, pp. 5620–5624, Oct. 2018.

[20] Y. J. Cheng, W. Hong, and K. Wu, "94 GHz substrate integrated monopulse antenna array," *IEEE Trans. Antennas Propag.*, vol. 60, no. 1, pp. 121–129, Jan. 2012.

[21] R. Harrington and J. Mautz, "Theory of characteristic modes for conducting bodies," *IEEE Trans. Antennas Propag.*, vol. AP-19, no. 5, pp. 622–628, Sep. 1971.

[22] CST Studio Suite. *Computer Simulation Technology*. [Online]. Available: https://www.cst.com

[23] Y. Li and K.-M. Luk, "Low-cost high-gain and broadband substrate-integrated-waveguide-fed patch antenna array for 60-GHz band," *IEEE Trans. Antennas Propag.*, vol. 62, no. 11, pp. 5531–5538, Nov. 2014.

[24] Y. Li, J. Wang, and K.-M. Luk, "Millimeter-wave multibeam aperture-coupled magnetoelectric dipole array with planar substrate integrated beamforming network for 5G applications," *IEEE Trans. Antennas Propag.*, vol. 65, no. 12, pp. 6422–6431, Dec. 2017.

[25] C. A. Balanis, *Antenna Theory: Analysis and Design*. Hoboken, NJ, USA: Wiley, 2016.

[26] Ansys Corp. *Hfss:High Frequency Structure Simulator Based on the Finite Element Method*. Accessed: Jan. 27, 2020. [Online]. Available: https://www.ansys.com

[27] W. Li, K. D. Xu, X. Tang, Y. Yang, Y. Liu, and Q. H. Liu, "Substrate integrated waveguide cavity-backed slot array antenna using high-order radiation modes for dual-band applications in *K*-band," *IEEE Trans. Antennas Propag.*, vol. 65, no. 9, pp. 4556–4565, Sep. 2017.

[28] T. Deckmyn, M. Cauwe, D. Vande Ginste, H. Rogier, and S. Agneessens, "Dual-band (28,38) GHz coupled quarter-mode substrate-integrated waveguide antenna array for next-generation wireless systems," *IEEE Trans. Antennas Propag.*, vol. 67, no. 4, pp. 2405–2412, Apr. 2019.

BOTAO FENG (Senior Member, IEEE) was born in Guangdong, China, in 1980. He received the B.S. and M.S. degrees in communication engineering from the Chongqing University of Posts and Telecommunications, Chongqing (CQUPT), China, in 2004 and 2009, respectively, and the Ph.D. degree in communication and information system from the Beijing University of Posts and Telecommunications (BUPT), Beijing, China, in 2015.

He joined the Dongguan Branch, Nokia Mobile Phones Ltd., China, as a Senior Communication Engineer, in 2004. From 2009 to 2012, he served as a Senior Research Fellow and a Chief Executive with the Guangdong Branch, China United Network Communications Company Ltd., where he received the award of Breakout Star of the Year, and the title of Technical Innovation Expert. He is currently a Postgraduate Advisor and a Postdoctoral Advisor with Shenzhen University, Guangdong, China. He is also the Head of the Laboratory of Wireless Communication, Antennas and Propagation, Shenzhen University, also the Deputy Director with the Department of Electronic Science and Technology, also the Director of the Joint Laboratory of Antenna and Electromagnetic Propagation, Shenzhen University—Rihai Communication Technology Company Ltd., also the Director of the Joint Laboratory of Shenzhen Zhongke Wireless Technology Company Ltd., and the Group of Wireless Communication, Antennas and Propagation, Shenzhen University, also the Director of the Joint Laboratory of Antenna and Microwave Technology, Shenzhen University—Skywave Communication Technology Company Ltd., also the Chief Scientist with Shenzhen Nandouxing Technology Company Ltd., and the President of Shenzhen Taobida Technology Company Ltd. His research team members are currently conducting more than 20 projects on antenna development and design for 5G/THz and future communications, which are supported by natural science research funds and industrial cooperation research and development funds. His several antenna designs for 5G applications have been widely used by Chinese communication operators. He has authored or coauthored more than 50 Science Citation Index (SCI)- and Engineering Index (EI)-articles, and holds more than 20 invention patents. It is estimated that the related total production value is approximately 200 million Ren Min Bi (RMB). His research interests include antennas and mobile communications.

Dr. Feng has obtained the award of the Outstanding Instructor of the First Prize in National Graduate Electronic Contest, and the Tencent Outstanding Teacher Award, since 2017. He also serves as a Regular Peer Reviewer, a Technical Committee Member, a Section Chair, and a Guest Editor of IEEE/IET, Elsevier, Wiley, and Springer journals and conferences on microwave technique and antenna development.

XIAOYUAN HE was born in Shanwei, Guangdong, China, in 1998. She received the B.S. degree from Shenzhen University, in 2019. She is currently pursuing the M.S. degree with the Beijing University of Posts and Telecommunications (BUPT), Beijing, China. Her research interests include the design of wideband antenna, base-station antenna, and millimeter wave antenna.

JUI-CHING CHENG was born in Taipei, Taiwan. He received the B.S. and M.S. degrees in electrical engineering from National Taiwan University, Taipei, Taiwan, in 1987 and 1989, respectively, and the Ph.D. degree in electrical engineering from the University of Michigan, Ann Arbor, MI, USA, in 1998.

From 1989 to 1991, he served in the R.O.C. Air Force as an Air Defense Artillery Officer. From 1991 to 1992, he was a Research Assistant with the Institute of Information Science, Academia Sinica, Taipei, Taiwan. From 1993 to 1997, he was a Graduate Research Assistant with the Radiation Laboratory, University of Michigan. From 1997 to 2001, he was a Senior Research Scientist with EMAG Technologies, Ann Arbor. From 2001 to 2013, he was a Faculty Member with the Department of Electronic Engineering, Chang Gung University. Since 2013, he has been a Faculty Member with the Department of Electronic Engineering, National Taipei University of Technology. His primary research interests include computational electromagnetics, antennas, and microwave circuits.

CHOW-YEN-DESMOND SIM (Senior Member, IEEE) was born in Singapore, in 1971. He received the B.Sc. degree from the Engineering Department, University of Leicester, U.K., in 1998, and the Ph.D. degree from the Radio System Group, Engineering Department, University of Leicester, in 2003.

From 2003 to 2007, he was an Assistant Professor with the Department of Computer and Communication Engineering, Chienkuo Technology University, Changhua, Taiwan. In 2007, he joined the Department of Electrical Engineering, Feng Chia University (FCU), Taichung, Taiwan, as an Associate Professor, where he became a Full Professor, in 2012 and as a Distinguished Professor, in 2017. He has served as the Executive Officer of Master's Program with the College of Information and Electrical Engineering (Industrial Research and Development), the Director of Intelligent IoT Industrial Ph.D. Program, from August 2015 to July 2018. He is currently serving as the Head of the Department of Electrical Engineering and also the Director of the Antennas and Microwave Circuits Innovation Research Center, Feng Chia University. He has authored or coauthored more than 130 SCI articles. His current research interests include antenna design, VHF/UHF tropospheric propagation, and RFID applications.

Prof. Sim is a Fellow of the Institute of Engineering and Technology (FIET), a Senior Member of the IEEE Antennas and Propagation Society, and a Life Member of the IAET. He served as the TPC Member of the APMC 2012, the APCAP 2015, IMWS-Bio 2015, CSQRWC 2016, ICCEM 2017, APCAP 2018, CIAP 2018, and APMC 2019. He was the recipient of the IEEE Antennas and Propagation Society Outstanding Reviewer Award (IEEE Transaction Antennas and Propagation) for six consecutive years, from 2014 to 2019. He has also served as the TPC Sub-Committee Chair (Antenna) of the ISAP 2014, PIERS 2017, and PIERS 2019. He was invited as the Workshop/Tutorial Speaker in APEMC 2015, iAIM 2017, InCAP 2018, and an Invited Speaker of TDAT 2015, iWAT 2018, APCAP 2018, and ISAP 2019. He has also served as the TPC Chair of the APCAP 2016 and iWEM 2019. He has served as the Chapter Chair of the IEEE AP-Society, Taipei Chapter, from 2016 to 2017. He has been the Founding Chapter Chair of the IEEE Council of RFID, Taipei Chapter, since 2017. He is currently serving as an Associate Editor of IEEE AWPL, IEEE Access, the IEEE Journal of RFID, and (Wiley) *International Journal of RF and Microwave Computer-Aided Engineering*. He has also received the Outstanding Associate Editor Award from the IEEE Antennas Wireless and Propagation Letters, in July 2018. He was the Keynote Speaker of SOLI 2018. He has served as the Advisory Committee of InCAP, from 2018 to 2019. Since October 2016, he has been serving as the Technical Consultant of Securitag Assembly Group (SAG), which is one of the largest RFID tag manufacturers in Taiwan.